3-D Imaging Using Row–Column-Addressed Arrays With Integrated Apodization—Part I: Apodization Design and Line Element Beamforming

Morten Fischer Rasmussen, Thomas Lehrmann Christiansen, Erik Vilain Thomsen, and Jørgen Arendt Jensen, *Fellow, IEEE*

***Abstract*—This paper investigates the effect of transducer-integrated apodization in row–column-addressed arrays and presents a beamforming approach specific for such arrays. Row–column addressing 2-D arrays greatly reduces the number of active channels needed to acquire a 3-D volume. A disadvantage of row–column-addressed arrays is an apparent ghost effect in the point spread function caused by edge waves. This paper investigates the origin of the edge waves and the effect of introducing an integrated apodization to reduce the ghost echoes. The performance of a $\lambda/2$-pitch 5-MHz 128 + 128 row–column-addressed array with different apodizations is simulated. A Hann apodization is shown to decrease imaging performance away from the center axis of the array because of a decrease in main lobe amplitude. Instead, a static roll-off apodization region located at the ends of the line elements is proposed. In simulations, the peak ghost echo intensity of a scatterer at $(x, y, z) = (8, 3, 30)$ mm was decreased by 43 dB by integrating roll-off apodization into the array. The main lobe was unaffected by the apodization. Simulations of a 3-mm-diameter anechoic blood vessel at 30 mm depth showed that applying the transducer-integrated apodization increased the apparent diameter of the vessel from 2.0 mm to 2.4 mm, corresponding to an increase from 67% to 80% of the true vessel diameter. The line element beamforming approach is shown to be essential for achieving correct time-of-flight calculations, and hence avoid geometrical distortions. In Part II of this work, experimental results from a capacitive micromachined ultrasonic transducer with integrated roll-off apodization are given to validate the effect of integrating apodization into the line elements.**

I. Introduction

For real-time 3-D ultrasonic imaging, 2-D array transducers are needed to achieve real-time scanning of a volume [1], [2]. The number of elements in a fully addressed 2-D array scales with N^2. In 2-D imaging, a 1-D array using more than 100 elements is commonly used. Using a fully addressed 2-D array, this would correspond to an array with more than 10 000 elements. To control the individual elements in the array, a connection must be made to each element. Thereby, any delay or apodization scheme can be applied, offering maximum control and flexibility in the image processing [2]–[4]. However, addressing each element individually results in a vast number of interconnections and offers a great challenge in acquiring and processing the large amount of data. Reducing the number of transducer elements by using sparse arrays has therefore received a great amount of interest in the last couple of decades [5]–[9]. One of the drawbacks of sparse arrays, however, is the lower emitted energy from the reduced number of elements, leading to a lower SNR in the recorded ultrasound image. The sparse arrays also have higher side lobes and can introduce grating lobes in the field.

2-D row–column-addressed arrays have recently attracted some attention [10]–[25]. In a row–column-addressed array, the elements are accessed by their row or column index. Each row and column in the array thereby acts as one large element. This effectively transforms the dense 2-D array into two orthogonal 1-D arrays, as illustrated in Fig. 1. Thereby, the number of elements in a 2-D array is reduced from N^2 to $2N$. The long elements are in this work referred to as row elements and column elements, or simply as line elements.

Considering a fully populated array with $N \times N$ elements, a row–column-addressed array of the same size would contain $N + N$ line elements. The size of one line element is then $1 \times N$, in units of the fully populated array elements. The vibrating surface area, when exciting a single row–column-addressed transducer array channel, is therefore N times as large as the excited area of the fully populated area. A row–column-addressed array therefore emits far more energy per transducer channel than a fully populated array. In [22], the resolution and contrast of row–column-addressed arrays is shown to be better than for fully addressed arrays, when they use the same number of active channels. The row–column-addressed array is a very interesting candidate for real-time 3-D imaging because it both has a large surface area and promises to achieve a high resolution per active channel. Although the row–column addressing scheme greatly reduces the

Manuscript received May 22, 2014; accepted March 19, 2015. This work was financially supported by grant 024-2008-3 and 82-2012-4 from the Danish Advanced Technology Foundation and from BK Medical ApS, Herlev, Denmark.

M. F. Rasmussen and J. A. Jensen are with the Center for Fast Ultrasound Imaging, Department of Electrical Engineering, Technical University of Denmark, Kgs. Lyngby, Denmark (e-mail: research@mofi.dk).

T. L. Christiansen and E. V. Thomsen are with the Department of Micro- and Nanotechnology, Technical University of Denmark, Kgs. Lyngby, Denmark.

DOI http://dx.doi.org/10.1109/TUFFC.2014.006531

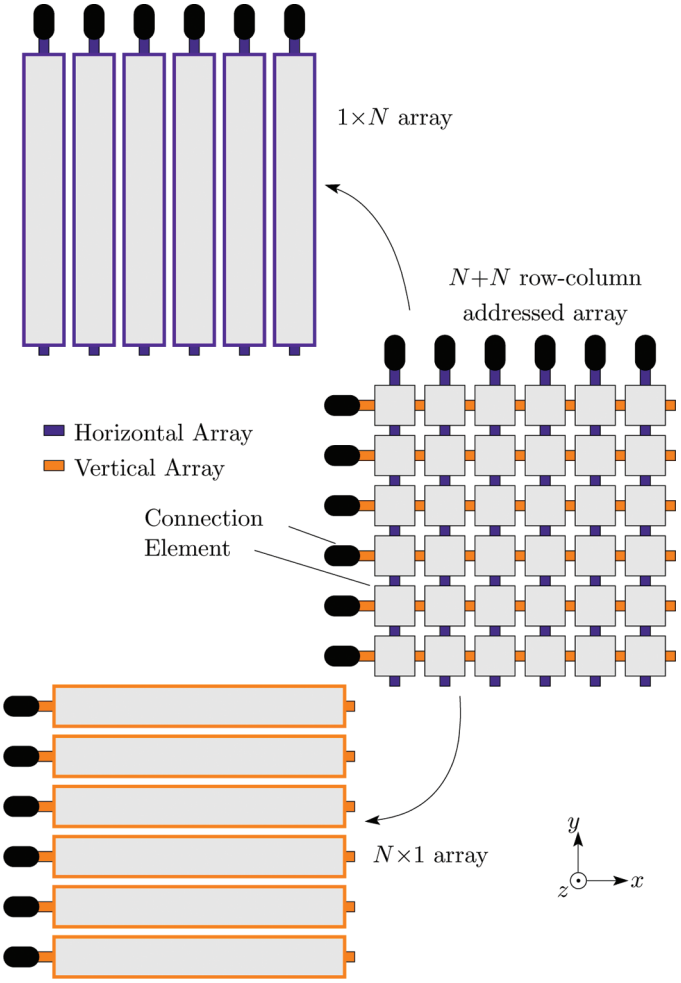

Fig. 1. A row–column-addressed 2-D transducer array can be interpreted as two orthogonal 1-D arrays. To the right is shown a 2-D transducer array, where each transducer element is addressed by its row or column index, effectively creating the two arrays shown to the left.

number of elements and beamformer channels needed to perform real-time 3-D imaging, it has one major disadvantage compared with the fully addressed 2-D arrays: the long row- and column-elements have considerably increased edge effects. As was shown in [22], the edge effect limits the image quality obtainable with 2-D row–column-addressed arrays. This paper demonstrates how these edge effects can be effectively reduced, making row–column-addressed arrays capable of providing a high image quality for real-time 3-D imaging with a low channel count.

The paper is divided into three main sections. The first section describes the edge effects of long, thin line elements, and demonstrates the importance of apodizing the line elements along their length to reduce the edge effects. Subsequently, a transducer-integrated apodization is designed. It is shown that the previously proposed apodization in the literature [19], [22] is not generally applicable for 3-D imaging. Instead, a new apodization scheme is proposed and simulated. Then, it is demonstrated how beamforming can be carried out when both the transmit line elements, the receive line elements, and the focal zone are line segments instead of points. Finally, the effectiveness of the proposed apodization is demonstrated via simulated point spread functions (PSFs) and a simulated anechoic blood vessel surrounded by tissue.

TABLE I. Simulation Parameters.

Parameter name	Notation	Value	Unit
Center frequency	f_0	5.0	MHz
Speed of sound	c	1480	m/s
Wavelength	λ	296	μm
Array pitch—x	d_x	$\lambda/2 = 148$	μm
Array pitch—y	d_y	$\lambda/2 = 148$	μm
Sampling frequency	f_s	120	MHz
Emission pulse	—	2-cycles, Hann-weighted	—

In Part II of this work [26], experimental results from a 62 + 62 element, $\lambda/2$-pitch, 2.77-MHz capacitive micromachined ultrasonic transducer with integrated apodization are given and compared with simulations of an array with identical properties. The array presented in Part II is a prototype, intended to experimentally validate the effect of the integrated apodization. To better illustrate the potential of a larger array, Part I includes simulations of a 128 + 128 element, $\lambda/2$-pitch, 5-MHz row–column-addressed transducer array.

II. Simulation Setup

In this work, Field II pro [27]–[29] is used for all simulations. The simulated receive signals are beamformed using a direct Matlab (The MathWorks Inc., Natick, MA, USA) implementation of the beamformer for row–column-addressed arrays presented in Section V. The transducer arrays used in the simulations are row–column-addressed 128 + 128 element 2-D arrays using the parameters shown in Table I. The orthogonal transmit and receive transducer array pairs are implemented as 1 × 128 and 128 × 1 2-D arrays. Each line element is divided into square mathematical sub-elements with a side length of $\lambda/4$.

III. Edge Effects

Row–column-addressed arrays are quite different acoustically from fully addressed arrays. Because of the row–column addressing, each line element may have a length that is hundreds of times longer than the lengths of the square elements used in a fully addressed array. The long length of the line elements results in prominent edge effects. This section investigates how the line elements of a row–column-addressed array behave and what can be done to decrease the edge effects. The behavior of the line elements is first investigated by analyzing their spatial impulse response.

A. Spatial Impulse Response

In the following, the importance of apodizing the line elements along their length is demonstrated. For this pur-

pose, an approximation to spatial impulse response is derived. The purpose of the derivation is not to introduce a new equation suitable for calculating the impulse response, but to elucidate how the edge effects can be minimized.

The origin of the edge waves can be analyzed by the linear theory of wave propagation. The pressure at a given point $\mathbf{p}$ at the time t has in the literature [30] been shown to be

$$p(\mathbf{p},t) = \rho_0 \frac{\partial}{\partial t} v(t) * h(\mathbf{p},t) \tag{1a}$$

$$= \rho_0 v(t) * \frac{\partial}{\partial t} h(\mathbf{p},t), \tag{1b}$$

where $*$ denotes temporal convolution, ρ_0 is the density of the medium, v is the velocity normal to the transducer surface, and h is the spatial impulse response. It is noted that v is the convolution of the aperture excitation signal and the electro-mechanical impulse response of the aperture. The spatial impulse response $h(\mathbf{p},t)$ is the observed sound field at the point $\mathbf{p}$ when the aperture is excited by a Dirac delta function. The Huygens–Fresnel principle states that the field originating from a sound radiating surface can be calculated by considering all points on the surface as the source of an expanding spherical wave. The field at any point in space is then constructed by superposition of these spherical waves. The acoustic reciprocity theorem states that if the sound source and the sound receiver are interchanged, the received signal remains unchanged. In other words, the spatial impulse response can be determined by letting the point $\mathbf{p}$ be the source of a spherical wavefront and then integrate the wave's intersection with the aperture. This integral is termed the Rayleigh integral [31], [32].

The intersection of the spherical wave and the plane of the aperture makes a circle arc. The spatial impulse response at a certain time t is thereby determined by the length of the arc that intersects the aperture. The radius of the expanding sphere is $R = ct$, where t is time and c is the speed of sound. Determining the arc intersection is reduced to a two-dimensional problem by projecting the point $\mathbf{p}$ onto the transducer plane. Without loss of generality, the aperture is assumed to be flat. In the following, a normal right-handed coordinate system consisting of x, y, and z coordinates is used. The aperture plane is spanned by the x- and y-axes and the z-axis is orthogonal to the aperture plane. If the coordinate of $\mathbf{p}$ is (p_x, p_y, p_z), then the projection of $\mathbf{p}$ onto the xy-plane is $(p_x, p_y, 0)$. The radius of the circle created by the intersection between the aperture and the expanding spherical wave is $\rho(t) = \sqrt{(ct)^2 - p_z^2}$ and the center of the circle is located at (p_x, p_y). The line integral along this expanding arc is the Rayleigh integral in polar coordinates. This is the case shown in the aperture at the top of Fig. 2. The integration is performed along the gray dashed lines. Several authors [33]–[35] have determined the solution to the Rayleigh integral in polar coordinates of an apodized aperture to be

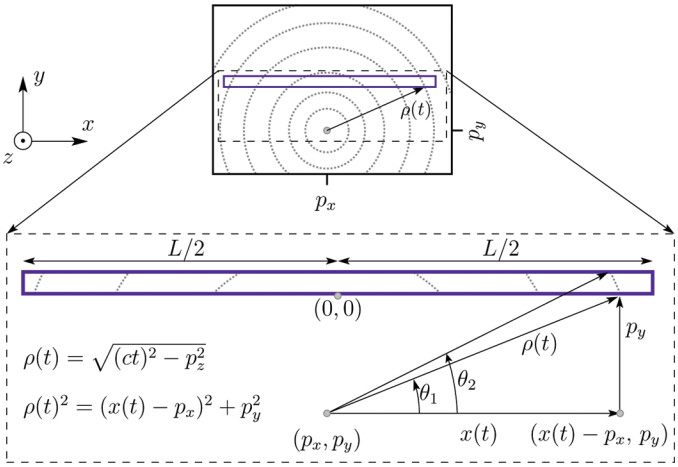

Fig. 2. Spatial impulse response of long, thin line elements. At the top a large aperture is shown with integration paths marked with gray dashed lines. The integration paths are used in (2) to determine the spatial impulse response. Within the large aperture, a thin line element is illustrated. At the bottom, a magnified image of the line element is shown. The expression in (5) approximates the integration paths with vertical lines. The thinner the line element is, the better the approximation.

$$h(\mathbf{p},t) = \begin{cases} \dfrac{c}{2\pi} \displaystyle\int_{\theta_1(t)}^{\theta_2(t)} a(\rho(t),\theta) \mathrm{d}\theta, & \text{if } t \geq \dfrac{p_z}{c} \\ 0, & \text{else,} \end{cases} \tag{2}$$

where a is the apodization function of the aperture in polar coordinates with origin at the projection of $\mathbf{p}$ onto the aperture plane. a is equal to 0 when evaluated outside of the aperture surface. If the apodization function is constant along the integration paths, (2) becomes

$$h(\mathbf{p},t) = \begin{cases} \dfrac{c}{2\pi} (\theta_2(t) - \theta_1(t)) a_\rho(\rho(t)), & \text{if } t \geq \dfrac{p_z}{c} \\ 0, & \text{else.} \end{cases} \tag{3}$$

In the following, the aperture is assumed to be a long, thin, and rectangular line element. The x, y-coordinates are chosen such that the x-axis is oriented along the length of the line element and the origin is placed at the center of the line element length. This is illustrated in Fig. 2.

At the top of Fig. 2, a large aperture is shown where the full integral along the dashed lines must be carried out to find the spatial impulse response. Within the large aperture, a line element is shown. A zoom on the line element is shown at the bottom of the figure. By approximating the integration paths on the line element by a vertical line, the apodization function $a_\rho(\rho)$ from (3) changes dependent variable from the radius ρ to the position x, representing the position along the line element: $a_x(x(t))$. The thinner the line element is, the better is the approximation. From the triangle at the bottom right in Fig. 2, the x-variable as a function of time is determined to:

$$x(t) = p_x \pm \sqrt{\rho(t)^2 - p_x^2} \tag{4a}$$

$$= p_x \pm \sqrt{(ct)^2 - p_z^2 - p_y^2}. \tag{4b}$$

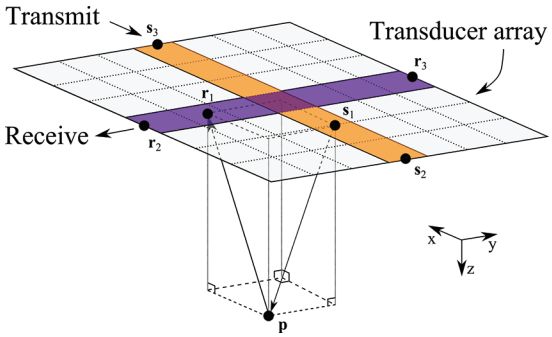

Fig. 3. Illustration of a pulse-echo simulation setup with one line element transmitting and one line element receiving. A scatterer is located at the point $\mathbf{p}$, $\mathbf{s}_1$ is the closest point on the transmit element to $\mathbf{p}$, and $\mathbf{r}_1$ is the closest point on the receive element to $\mathbf{p}$. $\mathbf{s}_2$, $\mathbf{s}_3$ and $\mathbf{r}_2$, $\mathbf{r}_3$ are the edges of the transmit and receive line elements, respectively.

The spatial impulse response then approximately becomes:

$$h(\mathbf{p},t) \approx \begin{cases} \frac{c}{2\pi}(\theta_2(t)-\theta_1(t))\, a_x(x(t)), & \text{if } t \geq t_1 \\ 0, & \text{else,} \end{cases} \tag{5}$$

where $t_1 = \sqrt{p_y^2 + p_z^2}/c$ is the earliest time at which the spherical wave arrives at the aperture. For a long, thin line element, the angular element width $(\theta_2(t) - \theta_1(t))$ changes much slower than the apodization function at the edges of the line element, i.e.,

$$\frac{\frac{\mathrm{d}}{\mathrm{d}t}(\theta_2(t)-\theta_1(t))}{2\pi} \ll \frac{\mathrm{d}}{\mathrm{d}t} a_x(x(t))\,. \tag{6}$$

By inserting (5) into (1b), and using (6), the pressure field is seen to be proportional to

$$p(\mathbf{p},t) \propto \begin{cases} v(t) * \frac{\mathrm{d}}{\mathrm{d}t} a_x(x(t)), & \text{if } t \geq t_1 \\ 0, & \text{else.} \end{cases} \tag{7}$$

Consider now the transmitting element of the row–column-addressed array shown in Fig. 3. Using the acoustic reciprocity, the pressure at point $\mathbf{p}$ can be found by assuming that $\mathbf{p}$ emits a spherical wavefront that is received by the transmitting line element. The wavefront reaches the closest point on the transmit line element ($\mathbf{s}_1$) at time $t = t_1$. At $t = t_2$, the wavefront first reaches the closest edge at $\mathbf{s}_2$, and at $t = t_3$, the wavefront reaches the furthest edge of the line element at $\mathbf{s}_3$. The apodization of a single line element is usually constant or only slowly varying over the entire element surface. Because the apodization function evaluates to zero outside of the element area, there is a discontinuity at the element edges at $\mathbf{s}_2$ and $\mathbf{s}_3$. The derivative of the aperture function is therefore approximately zero everywhere except at the discontinuities at $\mathbf{s}_1$, $\mathbf{s}_2$, and $\mathbf{s}_3$, where it is the Dirac delta function, δ:

$$\frac{\mathrm{d}}{\mathrm{d}t} a_x(x(t)) \approx \delta(t-t_1) - \delta(t-t_2) - \delta(t-t_3). \tag{8}$$

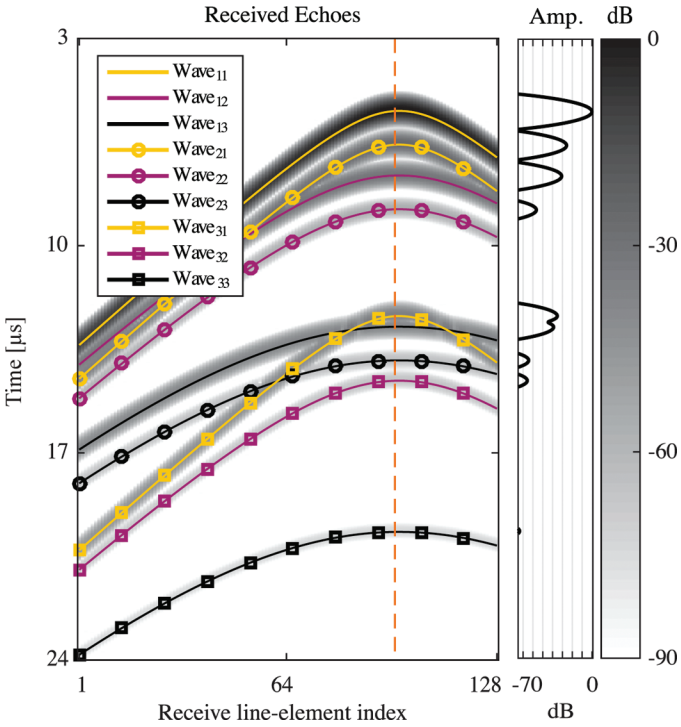

Fig. 4. Nine echoes are received from a single line element emission reflected by a scatter located at $(x, y, z) = (5, 4, 3)$ mm. The gray-scale image is the envelope of the received signals and the overlaid lines are predicted time-of-flights. The predicted time-of-flight is calculated using (9). The amplitudes of the echoes received by a single channel are plotted in the right sub-figure. The strongest ghost echo has an amplitude of −26 dB and the weakest ghost echo approximately −74 dB. That nine echoes are received exactly at the times predicted verifies the assumption that each line element behaves as three discrete elements, as illustrated in Fig. 3.

By inserting (8) into (7), it is seen that the spatial transmit impulse response contains three individual responses. As a result, a single transmit pulse develops three wavefronts that passes the point $\mathbf{p}$. When a scatterer is located at $\mathbf{p}$, there are therefore three reflected waves returning to the line element. Using the same argumentation, the spatial receive impulse response contains also three responses, meaning each wavefront is measured three times. The pulse-echo spatial impulse response is the convolution of the transmit and receive impulse responses and therefore contains up to nine responses. Referring to Fig. 3, the three wavefronts appear to originate from $\mathbf{s}_1$, $\mathbf{s}_2$, and $\mathbf{s}_3$. The receive line element behaves as if it measures at the three discrete points $\mathbf{r}_1$, $\mathbf{r}_2$, and $\mathbf{r}_3$. This analysis considered two out of four edges. The two long edges will also give rise to a response, but for elements with a width in the order of a wavelength, the two extra responses will merge with the $\mathbf{s}_1$ response and are therefore negligible.

That nine echoes are measured from a single scatterer can be tested by a single line element pulse-echo simulation. Fig. 4 shows the signals received by a 128 + 128 element row–column-addressed array from a single scatter located at the point $\mathbf{p} = (5, 4, 3)$ mm, when exciting the center line element with a two-cycle sinusoidal 5 MHz

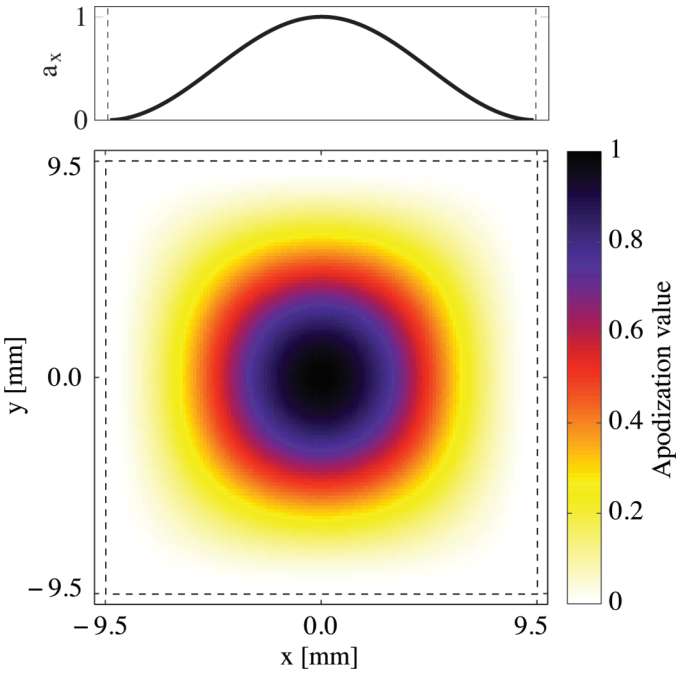

Fig. 5. The row–column-addressed array with a transducer-integrated Hann apodization. The graph at the top shows the Hann apodization of a single line element as a function of the position along the line element. The bottom figure shows the Hann apodization of the full transducer array. The dashed lines mark the edge of the line elements and the row–column-addressed array. The size of the area within the dashed lines is identical to that of the area within the dashed lines in Fig. 6.

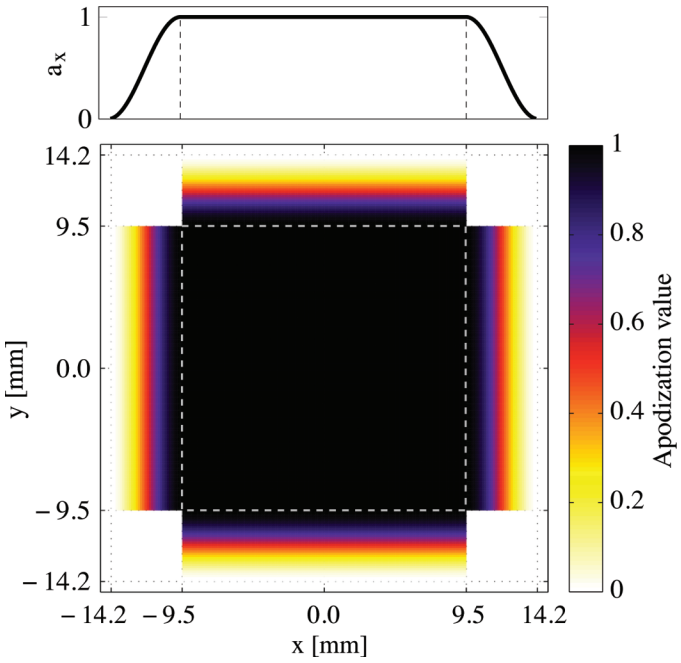

Fig. 6. New integrated-apodization layout where a roll-off region is added to the ends of the line elements. The graph at the top shows the apodization of each line element as a function of the position along the line element. The central region, marked with dashed lines, has an apodization value of one. The size of the area within the dashed lines is identical to that of the area within the dashed lines in Fig. 5.

pulse. As expected, nine echoes are received. Overlaid on the gray level receive echoes are the expected echo arrival time combinations of the three sources and the three receive points of Fig. 3. The echo arrival time, also termed the time-of-flight (ToF), is calculated as

$$\mathrm{ToF}(\mathbf{p}, n, i) = \frac{\|\mathbf{p} - \mathbf{s}_n\| + \|\mathbf{r}_i - \mathbf{p}\|}{c}, \tag{9}$$

where both n and i are indexes between 1 and 3. The wavefronts are named wave_{ni}, where n indicates the **s**-index and i indicates the **r**-index. It is seen that the arrival time at each receive line element of all received echoes are perfectly predicted, and the location assumption of the transmitter and receiver of each wavefront, shown in Fig. 3, must therefore be correct.

It is only the first echo, wave_{11}, that can be used for imaging, as the amplitudes of the other ghost echoes are too weak. The amplitude of the most powerful ghost echo is approximately 40 dB lower than the amplitude of the main echo. Even though the ghost echoes cannot be used for imaging, they still degrade the image quality. It is seen from (7) that to reduce the edge waves, and thereby the ghost echoes, the derivative of the apodization function must be kept as small as possible. The apodization function therefore must converge to zero when approaching the line element edges. This cannot be achieved by the usual electronic apodization, because this does not change the line element apodization value along the length of it. Instead, the apodization must be integrated into the transducer array itself, which is the subject of the following sections.

IV. Transducer-Integrated Apodization

Apodizing both the row and column line elements with a Hann function in the entire length of the line elements is very effective at suppressing the ghost echoes [19], [22]. A Hann apodized row–column-addressed array is shown in Fig. 5, where the top graph shows the apodization of a single line element. Because the row and column line elements are overlapping, so are their apodization functions. At each position on the transducer surface, two apodization functions are overlapping, one from a row element and one from a column element. The effective apodization is the multiplication of the two apodization functions. The vertical line elements close to the edges are multiplied by values close to zero by the horizontal apodization function. Similarly, the horizontal line elements at the edges are multiplied by values close to zero by the vertical apodization function. The sensitivity of the edge line elements is therefore highly limited. The only location where this apodization function allows the row–column-addressed array to perform well, is straight down at the center of the array. The output pressure of the Hann-apodized array is in an earlier study shown to be significantly lower than the output pressure of a non-apodized row–column-addressed transducer array [36]. Even if the array angles the trans-

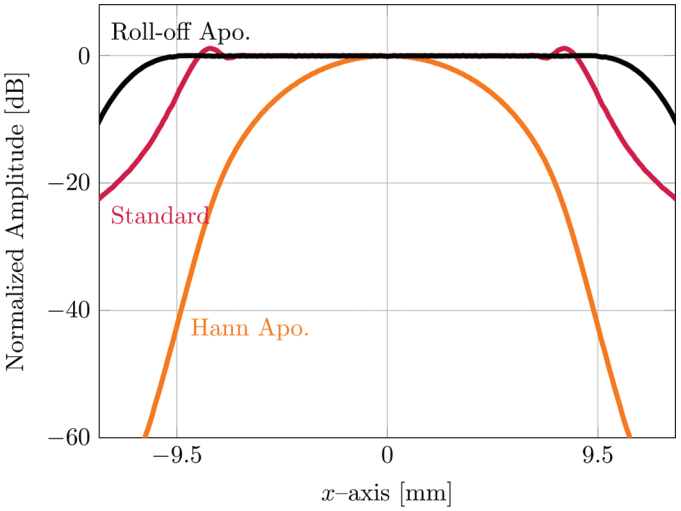

Fig. 7. Maximum received echo intensity from a single scatter at a depth of 10 mm and with its x-coordinate varying from −13 mm to 13 mm. The center line element is sending and all 128 receive elements are receiving. The maximum of all envelope-detected signals is plotted for each scatterer location. The three curves were simulated with three different apertures. The received signal acquired with an integrated Hann-apodized array is seen already to decrease quickly from the center of the array. The signal received with the standard array without any apodization decreases just before the edge of the array, and the roll-off-apodized array maintains the same signal strength until the edge of the array.

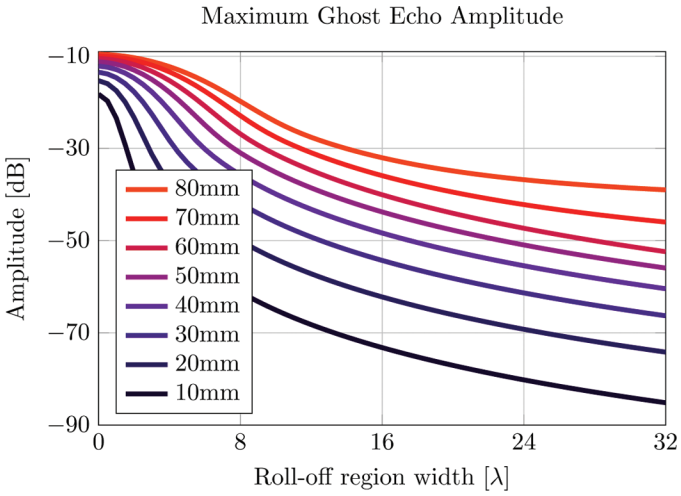

Fig. 8. Maximum ghost-echo intensity of a single scatterer as a function of edge apodization width. The wider the edge, the more the ghost echoes are suppressed. Each curve in the figure corresponds to a given scatterer depth, shown in the legend.

mit beam to the sides, like a phased array transducer, the echoes returning to the transducer surface will be significantly attenuated.

An alternative to the overlapping apodizations is to not apodize the central part of the transducer surface, but instead adding a roll-off region on both sides of all line elements, as shown in Fig. 6. This roll-off region is used for the apodization function to converge smoothly to zero. This way, the central region of the aperture surface has a uniform apodization value of 1, and there is no overlapping of the apodization functions where these are less than 1. At the same time, the discontinuities at the edges have been removed. If the added roll-off region is short, then the derivative of the aperture function will be high, and if the roll-off region is wide, the derivative will be low. From (7), it then follows that a wider roll-off region is better at suppressing the edge waves. Each line element thereby becomes longer, but there are the same number of row- and column-elements in the array. This apodization thereby does not affect the electronics, interconnections, or the data processing.

In Fig. 7, the simulated maximum received main echo as a function of scatterer position is shown. This expresses the array sensitivity as a function of position. The scatterer is placed directly in front of the transmitting line element at a depth of 10 mm. The center line element of the array emits a two-cycled pulse and the received echoes are measured on all receive line elements. The received signal is envelope detected and the maximum value is plotted against the scatterer position. The Hann-apodized array is seen to loose sensitivity very fast. At the edge of the array, the returned main echo is 40 dB weaker than in the center of the array. On the standard array without the integrated apodization, the Fresnel-diffraction of a sharp edge is evident close to the aperture edges at ±9.5 mm [37, p. 145]. The edge-apodized array has a constant sensitivity over entire central aperture, spanning from −9.5 mm to 9.5 mm in both dimensions. Adding roll-off regions to row–column-addressed arrays is therefore proposed as the standard solution.

In Fig. 8, the simulated maximum received ghost echo as a function of roll-off region width is shown. The scatterers are located at depths from 10 mm to 80 mm at the center of the aperture, where the ghost echoes reach their maximum amplitude. As expected, the wider the roll-off region is, the more the ghost echoes are suppressed. The deeper the scatter is located, the narrower is the effective width of the edge aperture, and its ghost-suppressing effect therefore decreases with depth. There is, however, an upper limit on the edge apodization width. A very large footprint results in difficulties getting a good acoustical contact between the aperture and the human body. For the rest of this paper, an edge width of 16λ is chosen as a compromise. 16λ is 1/4 of the original side length of 64λ, yielding a total aperture side length of 28.4 mm. As seen in Fig. 8, for a scatterer located at a depth of 10 mm, this will attenuate the ghost echo from −18 dB to −73 dB, and for a scatterer at 80 mm depth, this will attenuate the ghost echo from −10 dB to −32 dB. This corresponds to a damping of 55 dB and 22 dB, respectively. Importantly, this is without altering the electronics, interconnections, or data processing.

V. Beamforming With Line Sources

With a 1-D transducer array, focusing of the ultrasound wavefronts can be accomplished in the lateral direction.

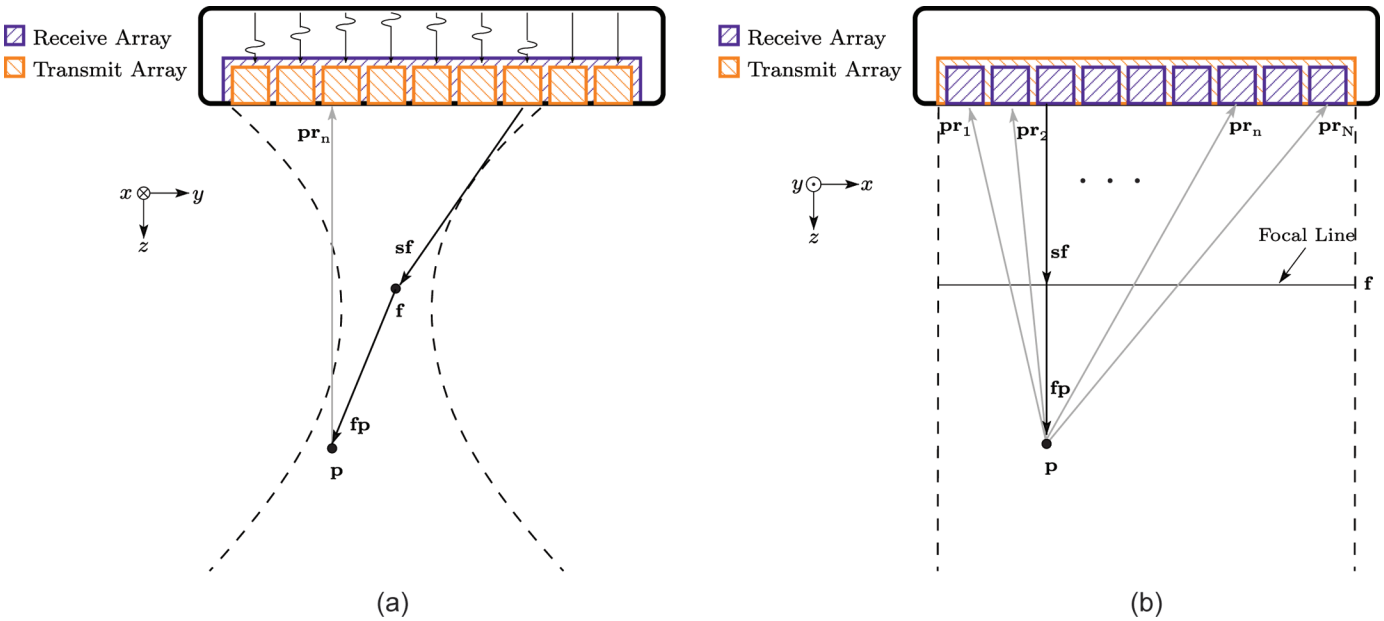

Fig. 9. Time of flight (ToF) illustration of a focused emission. The vector **sf** connects the first source line element that is excited with the focal line **f**. **fp** is the vector from the nearest point on the focal line to the point being beamformed (**p**), and $\mathbf{pr}_i$ is the vector from **p** to the nearest point on the receive line element $\mathbf{r}_i$. In (a) the setup is sliced orthogonal to the transmitting line elements and parallel with the receiving line elements, showing ToF in the y-dimension. In (b) the setup is sliced parallel with the transmitting line elements and orthogonal to the receiving line elements, showing ToF in the x-dimension. In (a) the focal zone **f** looks like a focal point, but in (b) it is seen to be a focal line.

In 2-D ultrasound imaging, the 1-D transmit and receive arrays are both used for focusing in the lateral direction. When focusing the ultrasound wavefronts using a row–column-addressed array, the transmit and receive arrays are orthogonal. This enables focusing of a 3-D volume, but the azimuth and elevation directions are only focused once [10], [18], [19], [22], [24].

Delay-and-sum beamformers usually assume the geometry of the sound sources and receivers to be points. The emitted wavefront of a line element has the shape of a cylindrical surface: it is a plane wave in the plane aligned along the line element and a circular arc in the plane orthogonal to the line element. Assuming the geometry of the line elements to be points is therefore a poor approximation. A better approximation assumes the line elements to be line segments. When an array of line elements is focused, the geometry of the focal zone is also a line segment. Calculating the distances between the line elements and a given point should therefore be calculated as the distance between a line segment and a point.

The vectors **fp** and $\mathbf{pr}_n$, seen in Fig. 9, connect the point **p** to the closest point on, respectively, the focal line **f** and the receiving element $\mathbf{r}_n$. **sf** is the vector from the source line element **s** to the focal line **f**. Because the source elements and the focal line are parallel, determining the distance between them can be solved in the zy-plane.

The time of flight of a wavefront is given by the shortest distance from the source **s** through the focal line **f** to the point being focused **p** and back to the receiving element $\mathbf{r}_n$, divided by the speed of sound. Using the notation from Fig. 9, this can be written as:

$$\mathrm{ToF}_m(\mathbf{p}, n) = \frac{\|\mathbf{sf}\| \pm \|\mathbf{fp}\| + \|\mathbf{pr}_n\|}{c}, \tag{10}$$

where c is the speed of sound in the medium, n is an index from 1 to the number of receive line elements N and m is the emission index. Only one value of ToF_m is calculated per emission. If the point being focused is closer to the transducer array than the focal line, then the case of $-||\mathbf{fp}||$ is used, otherwise $+||\mathbf{fp}||$ is used.

To determine $||\mathbf{fp}||$ and $||\mathbf{pr}_n||$, the distance between a point and line must be calculated. The line segment from point **a** to point **b** is termed **ab**. This is illustrated in Fig. 10. The projection of the point **p** onto the line **ab** is termed l and is determined by the usual equation for projection. l is positive if the projected point is located on the same side of **a** as **b**, and negative if it is located on the other side. By normalizing l with the length of the line segment, $\hat{l}$ takes the values $[0, 1]$ when the projected point is located between **a** and **b**:

$$\hat{l} = \frac{l}{\|\mathbf{ab}\|} = \frac{\mathbf{ap} \cdot \mathbf{ab}}{\|\mathbf{ab}\|^2}. \tag{11}$$

When the projection of **p** onto the line lies between **a** and **b**, i.e., when $\hat{l} \in [0, 1]$, the standard formula for the distance between a line and a point can be used:

$$d = \frac{||\mathbf{ab} \times \mathbf{ap}||}{||\mathbf{ab}||}. \tag{12}$$

When $\hat{l} \notin [0, 1]$, the shortest distance from the line segment to the point is the distance from the closest end of

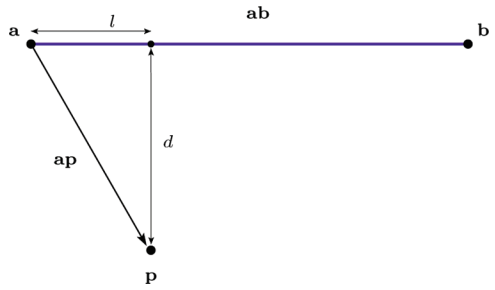

Fig. 10. Projection of the point **p** onto the line segment **ab**. l is the distance from **a** to the projected point and d is the shortest distance from **p** to **ab**.

the line segment (**a** or **b**) to the point (**p**). The following therefore determines the minimum distance between the point **p** and the line segment **ab**:

$$d(\mathbf{ab},\mathbf{p}) = \begin{cases} \dfrac{||\mathbf{ab}\times\mathbf{ap}||}{||\mathbf{ab}||} & \text{if } 0 \le \hat{l} \le 1 \\ ||\mathbf{ap}|| & \text{if } \hat{l} < 0 \\ ||\mathbf{bp}|| & \text{if } \hat{l} > 0. \end{cases} \tag{13}$$

Using (13), the distances $||\mathbf{fp}||$ and $||\mathbf{pr}_n||$ can now be determined as

$$||\mathbf{fp}|| = d(\mathbf{f},\mathbf{p}) \quad \text{and} \quad ||\mathbf{pr}_n|| = d(\mathbf{r}_n,\mathbf{p}). \tag{14}$$

By inserting (14) into (10), we arrive at

$$\text{ToF}_m(\mathbf{p},n) = \frac{||\mathbf{s}_{zy} - \mathbf{f}_{zy}||}{c} + \frac{d(\mathbf{r}_n,\mathbf{p}) \pm d(\mathbf{f},\mathbf{p})}{c}, \tag{15}$$

where $\mathbf{s}_{zy}$ and $\mathbf{f}_{zy}$ are the coordinates in the z-y plane of **s** and **f**, respectively. The focused signal at point **p** is calculated by summing all receive signals at the time instances given by (15):

$$s_m(\mathbf{p}) = \sum_{n=1}^{N} a_{\text{elec}}(n)\, y_{m,n}(\text{ToF}_m(\mathbf{p},n)), \tag{16}$$

where N is the number of receive elements, $a_{\text{elec}}(n)$ is the electronic receive apodization, and $y_{m,n}(t)$ is the measured signal from emission m on the receive element n at time t.

A Matlab beamformer that implements (16) was programmed to beamform data from row–column-addressed arrays and produce the point spread functions included in this paper. From (15), only the case in which $||\mathbf{fp}||$ is added is implemented, so that only points further away from the array than the focal line can be beamformed. The beamformer can IQ-beamform 250 000 voxels from a complex data set of 1.5 MiB from 128 receive line elements in approximately 11.4 on a PC with a 3.4-GHz Intel Core i7-3770 CPU (Intel Corp., Santa Clara, CA, USA) and 16 GiB of RAM. The proof-of-concept Matlab implementation of the beamformer can therefore not achieve a frame rate useful for real-time applications, but the frame rate is adequate for research purposes.

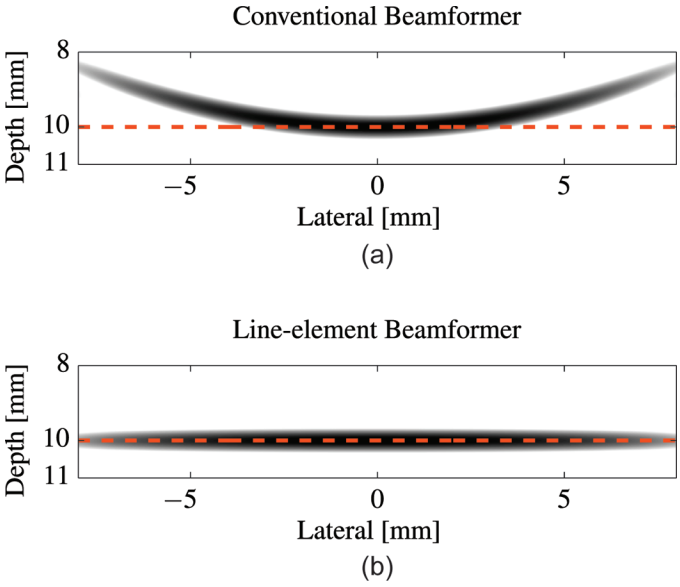

Fig. 11. B-mode images of a wire phantom beamformed (a) with a conventional beamformer and (b) with the proposed line-element beamformer. The dashed lines indicate the location of the wire phantom. The B-mode images are shown with a dynamic range of 40 dB. When using a conventional beamformer, the B-mode is seen to be geometrically distorted.

In Fig. 11, the importance of using a line-element beamformer is shown. In both figures, a wire phantom consisting of point scatterers located at 10 mm depth at the center of the transducer array is imaged. In Fig. 11(b), the line-element beamformer has been used, resulting in a reproduction of the wire with no geometrical distortions. In Fig. 11(a), conventional beamforming assuming point sources/receivers located at the center of the elements has been used. In this case the geometrical distortion of the wire caused by the error in the time-of-flight calculation is apparent, clearly demonstrating the need to take into consideration to the non-infinitesimal size of the sources/receivers.

VI. Image Quality

3-D rectilinear imaging can be achieved directly under the transducer array, marked with dashed lines in Fig. 6. The size of this area can be changed by varying number of transducer elements in the array and the pitch of the elements. The emission sequence can be designed exactly as when performing imaging with a 1-D transducer array.

A. Single-Element Emissions

In this work, a single-element emission sequence is used, leading to the use of 128 emissions for acquiring a full volume. Standard dynamic receive focusing is used to focus the lateral direction (x-dimension) and synthetic transmit focusing is used to dynamically focus the elevation direction (y-dimension) [38]–[41].

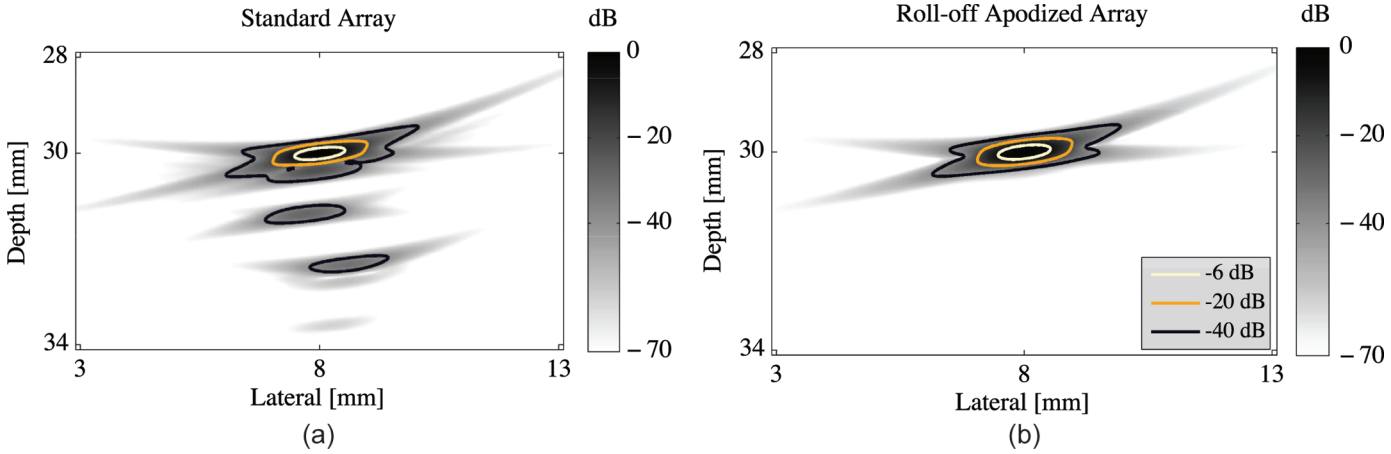

Fig. 12. PSF at $(x, y, z) = (8, 3, 30)$ mm: (a) the PSF of a standard non-apodized transducer array, and (b) the PSF of a transducer array with integrated roll-off apodization. The main responses of the PSFs are practically identical, but the ghost echoes of the roll-off-apodized array are greatly suppressed compared with the non-apodized standard array.

In Fig. 12, the PSF at $(x, y, z) = (8, 3, 30)$ mm, where 9 echoes are measured, is shown for both the standard and roll-off-apodized array. Because several of the ghost echoes arrive with a very short time interval, only 5 of the 8 ghost responses can be distinguished. The main response of the two arrays are almost identical, but the ghost echoes of the roll-off-apodized array are greatly suppressed compared with the non-apodized standard array. The maximum intensity of the PSFs in Fig. 12 is seen in Fig. 13 as a function of depth. The corresponding values for the Hann-apodized array has been added for comparison. The ghost responses seen on the PSF from the standard array are greatly attenuated by both the Hann-apodized array and the roll-off-apodized array. The maximum ghost echo is attenuated by 43 dB for the roll-off-apodized array and by 66.5 dB for the Hann-apodized array. On the other hand, the main response of the Hann-apodized array is seen to be attenuated by 24 dB, which clearly demonstrates the problem with the Hann apodization. As opposed to this, the roll-off-apodized array has preserved the amplitude of the main response. Taking the main response damping into consideration, the maximum ghost echo damping of the Hann-apodized array becomes 42.5 dB.

In Fig. 14, B-mode images of a simulated anechoic blood vessel are shown. The diameter of the blood vessel is 3 mm and both B-mode images were acquired using 128 single-line-element emissions [Fig. 14(a)] with a standard array and [Fig. 14(b)] with a roll-off-apodized array. The blood vessel phantoms used in Figs. 14(a) and 14(b) are identical, but the blood vessel in Fig. 14(a) appears smaller than the blood vessel in Fig. 14(b). The blood vessel diameter in Fig. 14(a) is decreased by the ghost echoes apparent when using the standard array. By determining the mean of the B-mode images in Fig. 14 along the x-dimension, the diameter of the blood vessel can be estimated. Defining the vessel wall as the location where the x-dimension mean crosses -20 dB, the blood vessel diameter is determined to be 2.4 mm and 2.0 mm for the apodized array and the standard array, respectively. This corresponds to 80% and 66.7% of the true vessel diameter, and shows how applying the transducer-integrated apodization increases the detectability of small anechoic objects. The imaging quality is therefore significantly better when the ghost echoes are removed by integrating roll-off apodization into the transducer array.

B. Phased-Array Imaging

The previous imaging examples were made using single-element emissions. To emphasize that the 1-D transmit array can be operated as a standard 1-D array, the following is an example of phased-array imaging. The vertical and horizontal arrays of the row–column-addressed 2-D array can each steer the transmit beam in one direction. In Fig. 15, the relative peak pressure is shown when steer-

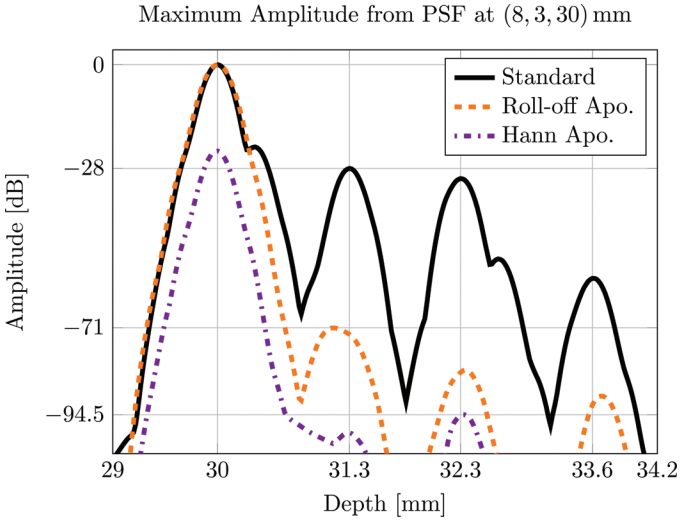

Fig. 13. Maximum intensity of the PSFs at $(x, y, z) = (8, 3, 30)$ mm as a function of depth. The Hann-apodized array is added for comparison. Both the roll-off-apodized array and the Hann-apodized array greatly suppress the ghost echoes, but the maximum intensity of the main response of the Hann-apodized array is 24 dB lower than the other two arrays.

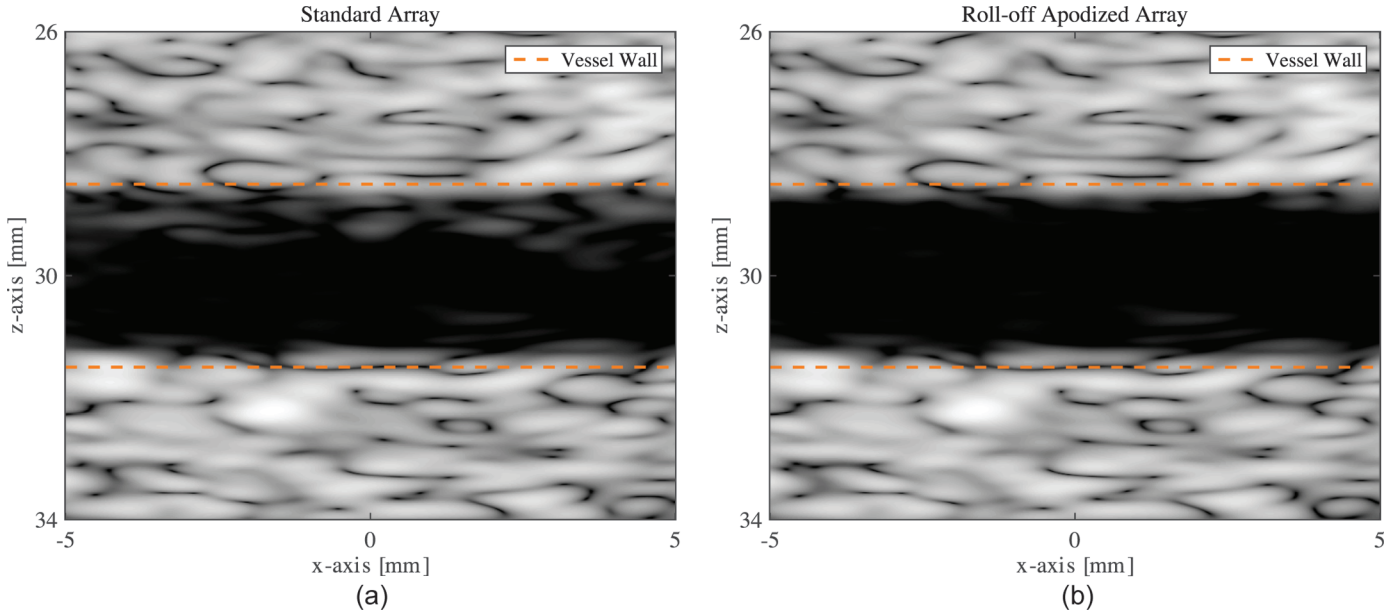

Fig. 14. B-mode images of a slice through the center of an anechoic blood vessel with a diameter of 3 mm located at 30 mm depth; (a) is made with a standard array and (b) with the roll-off-apodized array. The dynamic range is 40 dB for both images. Because of ghost echoes in the PSF for the standard array, the blood vessel in (a) appears to be smaller than the blood vessel in (b).

ing the transmit beam to the sides. For the phased-array transmit beam, all 128 elements were focused at a distance of 80 mm. The transmit beam was varied by $\pm 45°$ and each voxel in the figure is placed on the focal line for a given emission. 200 emissions were used to create Fig. 15. When the horizontal array is used as a transmit array, it can steer the transmit angle within in the *zx*-plane, and at the same time the vertical array is receiving. When the sequence has completed, the two arrays switch function, and now the vertical array is used as a transmit array. This leads to the energy being distributed as a cross, as seen in Fig. 15. Row–column-addressed arrays are therefore also well suited for cross-plane imaging. Full pyramid volume imaging can be achieved by defocusing the emitted energy using a curved array or an acoustic lens [10], [19]. When the transmit beam is steered to the side, the echoes arrive at the edge of the receive array first. To measure this signal, the roll-off region of the receive line elements must be disabled in that direction. For CMUTs, this can conveniently be achieved by simply removing the bias from the roll-off region. For piezo-element arrays, the roll-off region could be connected with switches to the line elements that then open when needed.

VII. Discussion and Conclusion

The spatial impulse response of thin line elements was shown to be proportional to the derivative of the line element's 1-D apodization function. The ghost echoes, apparent with row–column-addressed arrays, therefore originate from the discontinuity of the apodization function at the edge of the line elements. To minimize the ghost echoes, the derivative of the apodization functions must be minimized.

In the literature, it has previously been proposed to use the Hann apodization to minimize the ghost echoes. In this work, it was shown that using the Hann apodization has the disadvantage of emitting and receiving little energy off-center. Instead, it was proposed to add a transducer-integrated roll-off apodization region to the ends of the line elements. This way, the apodization functions of the horizontal and vertical line elements do not overlap when they differ from the apodization value of 1. The entire central region can thereby emit and receive at full strength. It was shown that a wider roll-off region leads to better ghost echo attenuation. A roll-off region width of

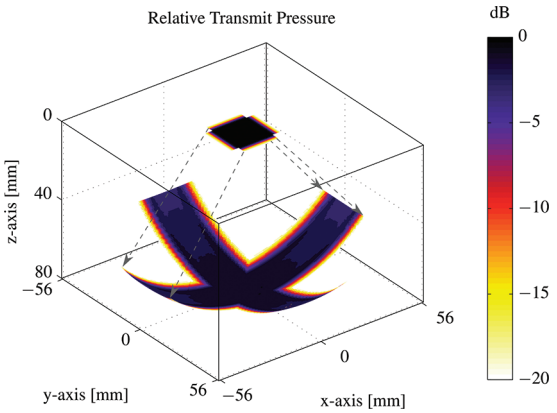

Fig. 15. Peak pressure distribution of a phased row–column-addressed array. The transmit array of the row–column-addressed array is used as a normal 1-D phased array from 2-D ultrasound imaging. Each voxel representing the pressure is located within the focal line. 200 emissions are used for simulating the figure and all 128 elements are excited during each emission. Each emission focuses at a different focal angle, but the focal distance is kept constant. For the pressure field to attain the cross shape shown in the figure, the transmit and receive arrays are interchanged after 100 emissions. This enables beamforming of cross-planes.

16λ was chosen, which led to a ghost echo damping in the PSF at $(x, y, z) = (8, 3, 30)$ mm of 43 dB. This rendered the ghost echoes invisible within the 70 dB dynamic range.

It was shown how data from a row–column-addressed array with a focal line can be delay-and-sum beamformed. The focal line can be located both in front of the array and behind it, and thereby both focused and unfocused emissions can be beamformed. A beamformer that can IQ-beamform 250 000 voxels from one emission in 11.4 s on a standard PC was presented.

Simulations of a 3-mm-diameter anechoic blood vessel at 30 mm depth showed that applying the transducer-integrated apodization increased the apparent diameter of the vessel from 2.0 mm to 2.4 mm. This corresponds to an increase from 67% to 80% of the true vessel diameter, and shows how applying the transducer-integrated apodization increases the detectability of small anechoic objects. The imaging quality is therefore improved when the ghost echoes are removed by integrating roll-off apodization into the transducer array.

In Part II of this work, experimental results from a CMUT array with integrated roll-off apodization are presented to validate the effect of integrating apodization into the line elements.

References

[1] O. T. von Ramm, S. W. Smith, and H. R. Pavy, "High speed ultrasound volumetric imaging system—Part II: Parallel processing and image display," *IEEE Trans. Ultrason. Ferroelectr. Freq. Control*, vol. 38, no. 2, pp. 109–115, 1991.

[2] D. H. Turnbull and F. S. Foster, "Beam steering with pulsed two-dimensional transducer arrays," *IEEE Trans. Ultrason. Ferroelectr. Freq. Control*, vol. 38, no. 4, pp. 320–333, Jul. 1991.

[3] K. E. Thomenius, "Evolution of ultrasound beamformers," in *Proc. IEEE Ultrason. Symp.*, 1996, vol. 2, pp. 1615–1621.

[4] G. R. Lockwood, J. R. Talman, and S. S. Brunke, "Real-time 3-D ultrasound imaging using sparse synthetic aperture beamforming," *IEEE Trans. Ultrason. Ferroelectr. Freq. Control*, vol. 45, no. 4, pp. 980–988, 1998.

[5] R. E. Davidsen, J. A. Jensen, and S. W. Smith, "Two-dimensional random arrays for real time volumetric imaging," *Ultrason. Imaging*, vol. 16, no. 3, pp. 143–163, Jul. 1994.

[6] S. S. Brunke and G. R. Lockwood, "Broad-bandwidth radiation patterns of sparse two-dimensional vernier arrays," *IEEE Trans. Ultrason. Ferroelectr. Freq. Control*, vol. 44, no. 5, pp. 1101–1109, Sep. 1997.

[7] J. T. Yen, J. P. Steinberg, and S. W. Smith, "Sparse 2-D array design for real time rectilinear volumetric imaging," *IEEE Trans. Ultrason. Ferroelectr. Freq. Control*, vol. 47, no. 1, pp. 93–110, Jan. 2000.

[8] A. Austeng and S. Holm, "Sparse 2-D arrays for 3-D phased array imaging—Design methods," *IEEE Trans. Ultrason. Ferroelectr. Freq. Control*, vol. 49, no. 8, pp. 1073–1086, Aug. 2002.

[9] M. Karaman, I. O. Wygant, O. Oralkan, and B. T. Khuri-Yakub, "Minimally redundant 2-D array designs for 3-D medical ultrasound imaging," *IEEE Trans. Med. Imaging*, vol. 28, pp. 1051–1061, Jul. 2009.

[10] C. E. Morton and G. R. Lockwood, "Theoretical assessment of a crossed electrode 2-D array for 3-D imaging," in *Proc. IEEE Ultrason. Symp.*, 2003, pp. 968–971.

[11] N. M. Daher and J. T. Yen, "Rectilinear 3-D ultrasound imaging using synthetic aperture techniques," in *Proc. IEEE Ultrason. Symp.*, 2004, vol. 2, pp. 1270–1273.

[12] N. M. Daher and J. T. Yen, "2-D array for 3-D ultrasound imaging using synthetic aperture techniques," *IEEE Trans. Ultrason. Ferroelectr. Freq. Control*, vol. 53, no. 5, pp. 912–924, 2006.

[13] C. H. Seo and J. T. Yen, "64 × 64 2-D array transducer with row–column addressing," in *Proc. IEEE Ultrason. Symp.*, 2006, vol. 1, pp. 74–77.

[14] C. H. Seo and J. T. Yen, "256 × 256 2-D array transducer with row–column addressing for 3-D imaging," in *Proc. IEEE Ultrason. Symp.*, 2007, pp. 2381–2384.

[15] C. H. Seo and J. T. Yen, "Recent results using a 256 × 256 2-D array transducer for 3-D rectilinear imaging," in *Proc. IEEE Ultrason. Symp.*, 2008, vol. 1–4, pp. 1146–1149.

[16] S. I. Awad and J. T. Yen, "3-D spatial compounding using a row–column array," *Ultrason. Imaging*, vol. 31, no. 2, pp. 120–130, 2009.

[17] A. S. Logan, L. L. P. Wong, and J. T. W. Yeow, "2-D CMUT wafer bonded imaging arrays with a row–column addressing scheme," in *Proc. IEEE Ultrason. Symp.*, 2009, pp. 984–987.

[18] C. H. Seo and J. T. Yen, "A 256 × 256 2-D array transducer with row–column addressing for 3-D rectilinear imaging," *IEEE Trans. Ultrason. Ferroelectr. Freq. Control*, vol. 56, no. 4, pp. 837–847, Apr. 2009.

[19] C. E. M. Démoré, A. Joyce, K. Wall, and G. Lockwood, "Real-time volume imaging using a crossed electrode array," *IEEE Trans. Ultrason. Ferroelectr. Freq. Control*, vol. 56, no. 6, pp. 1252–1261, 2009.

[20] A. S. Logan, L. L. P. Wong, A. I. H. Chen, and J. T. W. Yeow, "A 32 × 32 element row–column addressed capacitive micromachined ultrasonic transducer," *IEEE Trans. Ultrason. Ferroelectr. Freq. Control*, vol. 58, no. 6, pp. 1266–1271, Jun. 2011.

[21] A. I. H. Chen, L. L. Wong, A. S. Logan, and J. T. W. Yeow, "A CMUT-based real-time volumetric ultrasound imaging system with row–column addressing," in *Proc. IEEE Ultrason. Symp.*, 2011, pp. 1755–1758.

[22] M. F. Rasmussen and J. A. Jensen, "3D ultrasound imaging performance of a row–column addressed 2D array transducer: A simulation study," in *Proc. SPIE Med. Imag.*, 2013, art. no. 86750C.

[23] M. F. Rasmussen and J. A. Jensen, "3-D ultrasound imaging performance of a row–column addressed 2-D array transducer: A measurement study," in *Proc. IEEE Ultrason. Symp.*, 2013, pp. 1460–1463.

[24] J. T. Yen, "Beamforming of sound from two-dimensional arrays using spatial matched filters," *J. Acoust. Soc. Am.*, vol. 134, no. 5, pp. 3697–3704, Nov. 2013.

[25] A. Sampaleanu, P. Zhang, A. Kshirsagar, W. Moussa, and R. Zemp, "Top-orthogonal-to-bottom-electrode (TOBE) CMUT arrays for 3-D ultrasound imaging," *IEEE Trans. Ultrason. Ferroelectr. Freq. Control*, vol. 61, no. 2, pp. 266–276, 2014.

[26] T. L. Christiansen, M. F. Rasmussen, J. P. Bagge, L. N. Moesner, J. A. Jensen, and E. V. Thomsen, "3-D imaging using row–column-addressed arrays with integrated apodization—Part II: Transducer fabrication and experimental results," *IEEE Trans. Ultrason. Ferroelectr. Freq. Control*, vol. 62, no. 5, pp. 959–971, 2015.

[27] J. A. Jensen and N. B. Svendsen, "Calculation of pressure fields from arbitrarily shaped, apodized, and excited ultrasound transducers," *IEEE Trans. Ultrason. Ferroelectr. Freq. Control*, vol. 39, no. 2, pp. 262–267, 1992.

[28] J. A. Jensen, "Field: A program for simulating ultrasound systems," *Med. Biol. Eng. Comput.*, vol. 34, suppl. 1, pt. 1, pp. 351–353, 1996.

[29] J. A. Jensen, "A multi-threaded version of Field II," in *Proc. IEEE Ultrason. Symp.*, 2014, pp. 2229–2232.

[30] A. D. Pierce, *Acoustics, An Introduction to Physical Principles and Applications*. New York, NY, USA: Acoustical Society of America, 1989.

[31] P. R. Stepanishen, "Transient radiation from pistons in an infinite planar baffle," *J. Acoust. Soc. Am.*, vol. 49, no. 5B, pp. 1629–1638, 1971.

[32] G. R. Harris, "Review of transient field theory for a baffled planar piston," *J. Acoust. Soc. Am.*, vol. 70, no. 1, pp. 10–20, 1981.

[33] G. R. Harris, "Transient field of a baffled planar piston having an arbitrary vibration amplitude distribution," *J. Acoust. Soc. Am.*, vol. 70, no. 1, pp. 186–204, 1981.

[34] P. R. Stepanishen, "Acoustic transients from planar axisymmetric vibrators using the impulse response approach," *J. Acoust. Soc. Am.*, vol. 70, no. 4, pp. 1176–1181, 1981.

[35] J. Naze Tjøtta and S. Tjøtta, "Nearfield and farfield of pulsed acoustic radiators," *J. Acoust. Soc. Am.*, vol. 71, no. 4, pp. 824–834, 1982.

[36] T. L. Christiansen, M. F. Rasmussen, J. A. Jensen, and E. V. Thomsen, "Row–column addressed 2-D CMUT arrays with integrated apodization," in *Proc. IEEE Ultrason. Symp.*, 2014, pp. 600–603.

[37] P. V. Naik. *Principles of Physics*, 4th ed., Upper Saddle River, NJ, USA: Prentice Hall, 2010.

[38] J. T. Ylitalo and H. Ermert, "Ultrasound synthetic aperture imaging: Monostatic approach," *IEEE Trans. Ultrason. Ferroelectr. Freq. Control*, vol. 41, no. 3, pp. 333–339, 1994.
[39] M. Karaman, P. C. Li, and M. O'Donnell, "Synthetic aperture imaging for small scale systems," *IEEE Trans. Ultrason. Ferroelectr. Freq. Control*, vol. 42, no. 3, pp. 429–442, 1995.
[40] C. H. Frazier and W. D. O'Brien, "Synthetic aperture techniques with a virtual source element," *IEEE Trans. Ultrason. Ferroelectr. Freq. Control*, vol. 45, no. 1, pp. 196–207, 1998.
[41] M. F. Rasmussen and J. A. Jensen, "Comparison of 3-D synthetic aperture phased array ultrasound imaging with parallel beamforming," *IEEE Trans. Ultrason. Ferroelectr. Freq. Control*, vol. 61, no. 10, pp. 1638–1650, 2014.

Morten F. Rasmussen was born in 1981. He received the B.Sc., M.Sc., and Ph.D. degrees in electrical engineering from the Technical University of Denmark (DTU) in 2008, 2011, and 2014, respectively. In 2007, he spent ten months at the Technische Universität Berlin, Berlin, Germany, working on the BeeSat satellite. He is currently a postdoctoral research fellow at Stanford University. His current research interests include 3-D ultrasound imaging, synthetic aperture imaging techniques, and ultrasound neuro-stimulation.

Thomas Lehrmann Christiansen received his B.Sc. and M.Sc. degrees with honors in engineering physics and nanotechnology from the Technical University of Denmark, Kgs. Lyngby, Denmark, in 2010 and 2012, respectively. He is presently pursuing a Ph.D. degree at the Technical University of Denmark, focusing on micromachined ultrasonic transducers for three-dimensional imaging. He received the Oticon award in 2011 and the Danish Engineering Society's award in 2012 for his work on injection-molded microfluidic devices for automated patch-clamping. In 2014, he received the Elite-Forsk travel grant awarded to twenty selected Ph.D. students by the Danish Ministry of Higher Education and Science.

Erik V. Thomsen is a Professor at DTU Nanotech, the Technical University of Denmark, where he is heading the MEMS Applied Sensors group. He was born in Aarhus in 1964. He received the M.Sc. degree in physics from Odense University, Odense, Denmark, and the Ph.D. degree in electrical engineering from the Technical University of Denmark (DTU), Lyngby, in 1998. His current research and teaching interests include capacitive micromachined ultrasonic transducers, MEMS multisensors, biomedical devices, and small-scale energy systems such as miniature fuel cells and energy harvesting devices. He teaches classes in solid-state electronics, microtechnology, and nano- and microfabrication. Dr. Thomsen received the AEG Electron Prize in 1995 and has also received several teaching awards at DTU.

Jørgen Arendt Jensen earned his M.Sc. degree in electrical engineering in 1985 and his Ph.D. degree in 1989, both from the Technical University of Denmark. He received the Dr.Techn. degree from the same university in 1996. He has published more than 400 journal and conference papers on signal processing and medical ultrasound and the book *Estimation of Blood Velocities Using Ultrasound*, published by Cambridge University Press in 1996. He is also the developer of the Field II simulation program. He has been a visiting scientist at Duke University, Stanford University, and the University of Illinois at Urbana-Champaign. He is currently full professor of biomedical signal processing at the Technical University of Denmark in the Department of Electrical Engineering, and head of the Center for Fast Ultrasound Imaging. He has given courses on blood velocity estimation at both Duke University and the University of Illinois, and teaches biomedical signal processing and medical imaging at the Technical University of Denmark. He has given several short courses on simulation, synthetic aperture imaging, and flow estimation at international scientific conferences. He has received several awards for his research and is an IEEE Fellow. His research is centered on simulation of ultrasound imaging, synthetic aperture imaging, vector blood flow estimation, and construction of ultrasound research systems.